JOURNAL OF PROPULSION AND POWER
Vol. 24, No. 3, May–June 2008

Investigation of Two-Dimensional Scramjet Inlet Flowfield at Mach 7

J. Häberle* and A. Gülhan†
German Aerospace Center (DLR), 51147 Cologne, Germany

DOI: 10.2514/1.33545

A measurement campaign has been carried out to investigate the viscous flow effects in a fixed geometry two-dimensional scramjet inlet at Mach 7. The tests have been performed in a hypersonic blowdown wind-tunnel facility. The existing boundary layer separation due to shock interaction in the inlet throat can lead to inlet unstart. Therefore, an optional passive boundary layer bleed has been integrated at the throat. The passive bleed reduces the lip shock induced separation bubble in the throat significantly. The obtained experimental wall pressure distribution and pitot pressure profiles are discussed and compared to 2-D and 3-D computational fluid dynamics calculations. To investigate the compression behavior, different backpressure ratios have been applied to the isolator flow and the effects on the internal flow structure are analyzed by means of shadowgraph pictures, static pressure distribution, and pitot pressure profiles at the exit of the isolator. The heat transfer coefficient to the inner side wall of the isolator is calculated using the time-dependent surface temperature, measured with an infrared system. The resulting 2-D Stanton number distributions are presented for different configurations and different backpressure ratios. In addition, three different Reynolds numbers have been used to investigate the effect on the separation bubble located in the corner of the first and second ramp transitions and the resulting change in ramp heat flux.

Nomenclature

A	=	area, m^2
Bi	=	Biot number, $Bi = \alpha L_0 \cdot \lambda^{-1}$
C_P	=	specific heat capacity at constant pressure, $J \cdot kg^{-1} \cdot K^{-1}$
C_V	=	specific heat capacity at constant volume, $J \cdot kg^{-1} \cdot K^{-1}$
c_p	=	pressure coefficient, $c_P = (p - p_\infty) \cdot q_\infty^{-1}$
I	=	internal compression, $I = 1 - (A_{th} \cdot A_{lip}^{-1})$
L	=	length, m
M	=	Mach number
$\dot{m}$	=	mass flow, $kg \cdot s^{-1}$
Pr	=	Prandtl number
p	=	pressure, $N \cdot m^{-2}$
q	=	dynamic pressure, $N \cdot m^{-2}$
$\dot{q}$	=	heat flux rate, $W \cdot m^{-2}$
R	=	specific gas constant for air $R = 287.15$, $J \cdot kg^{-1} \cdot K^{-1}$
Re	=	Reynolds number
St	=	Stanton number, $St = \dot{q}_{conv} \cdot [\rho_\infty v_\infty c_{P,air}(T_{rec} - T_w)]^{-1}$
T	=	temperature, K
T_r	=	recovery temperature, $T_r = \lfloor 1 + r \cdot 0.5(\kappa - 1)M_\infty^2 \rfloor T_\infty$
W	=	width of the isolator, mm
α	=	heat transfer coefficient $W \cdot m^{-2} \cdot K^{-1}$, calibration value
Δ	=	throttle degree, $\Delta = \lfloor 1 - (A_{mfm,th} \cdot A_0^{-1}) \rfloor 100$, %
η_{KE}	=	kinetic energy efficiency
λ	=	heat conductivity, $W \cdot m^{-1} \cdot K^{-1}$
π	=	total pressure recovery, $\pi = p_{t3}/p_{t0}$
ρ	=	density, $kg \cdot m^{-3}$

Subscripts

CC	=	combustion chamber
conv.	=	convective
mfm	=	mass-flow meter
th	=	throat
$t0$	=	wind-tunnel total conditions
w	=	wall
∞	=	wind-tunnel freestream conditions

I. Introduction

FOR future hypersonic single-stage-to-orbit (SSTO) and two-stage-to-orbit (TSTO) vehicles for the access to space or hypersonic transportation, the propulsion unit is one of the critical subsystems [1]. Thus the emerging flow phenomena still have to be investigated in more detail to broaden the aerothermal database and to enable a reliable design. In continuation of previous hypersonic inlet investigations performed with different models, a newly designed hypersonic inlet compression system for a flight Mach number of $M = 7.5$–8 has been tested at $M = 7$ wind-tunnel conditions. The newly designed model is equipped with a higher geometrical resolution in static pressure ports and better optical access compared to the previous model [2]. This work is part of a research training group established to design a complete scramjet propulsion unit, that is, inlet, combustion chamber, and nozzle.

This paper focuses on the results of the internal compression part of a mixed compression hypersonic inlet, that is, the isolator and the throat area, because the internal flowpath features very complex flow phenomena, that is, shock–shock and shock-boundary layer interaction as discussed and illustrated, for example, in Herrmann and Reinartz [3,4] for an inlet-type setup. The varying shock structures and shapes in a squared duct with homogeneous inflow conditions are discussed by Sugiyama et al. [5]. The inlet is based on a 2-D double wedge ramp configuration with a horizontal lip. The geometry was designed by the method of characteristics (MOC) using an existing tool developed by Anderson [6]. The outward deflected flow is turned back into the freestream direction by a single lip shock. The relatively strong lip shock impinging on the ramp boundary layer results in a separation of the boundary layer, because the pressure gradient in the x direction is too large. As a consequence, a large separation bubble emerges in the throat of the inlet. This separation bubble causes pressure losses and, more important, the risk of blocking the inlet at flight conditions. This can occur at

Presented as Paper 5068 at the 43rd Joint Propulsion Conference, Cincinnati, Ohio, 8–11 July 2007; received 30 July 2007; revision received 18 December 2007; accepted for publication 21 December 2007.

*Ph.D. Student, Wind Tunnel Department of the Institute of Aerodynamic and Flow Technology, Linder Höhe D-51147 Köln. Student Member AIAA.

†Head of Department, Wind Tunnel Department of the Institute of Aerodynamic and Flow Technology, Linder Höhe D-51147 Köln. Member AIAA.

different angles of attack, real flight total temperature, and total pressure conditions, as well as for different ratios of wall-to-freestream temperature, depending on the different boundary layer development [7]. For all flight cases an inlet unstart, caused by the separation bubble, must be avoided.

In the model design a passive boundary layer bleed is integrated into the throat area as an option to reduce the separation bubble if blocking occurs at different flow conditions. The effects of this bleed on the flow structure and the necessity of such a device will be discussed in this paper.

Downstream of the inlet throat the isolator connects the inlet with the combustion chamber and adapts the flow in terms of static pressure delivered by the inlet to the static pressure in the combustion chamber. This is accomplished by a so-called shock train, a system of oblique or normal shocks. The fundamental description of the flow and the development of an engineering relationship for isolator design is reported by Billig [8,9] and in the standard work of Heiser and Pratt [10]. Depending on the combustion-chamber static pressure the flow structure in the isolator varies. These different structures are investigated and discussed in this paper by means of pitot pressure measurements, static pressure measurements, and a shadowgraph technique. In contrast to the assumed symmetric inflow conditions to the isolator in the above sited references the flow structure differs for the investigated inlet configuration. This is especially evident by comparing the pitot pressure profiles, for example, reported by Lin et al. [11] for different backpressure ratios with the here presented ones.

Because the thermal loads of a scramjet propulsion unit are very severe, reliable and detailed information about the heat loads acting on the different surfaces of a scramjet compression system are needed. A database for 2-D Stanton number distribution within the isolator is important and only limited information is available [12,13]. Thus the heat transfer coefficients on the isolator side walls are calculated by means of infrared thermography for a larger area of the internal flowpath than in the previous paper [2]. Moreover, the infrared thermography has been used to investigate the flow structure and the heat loads on the first and second external ramps with special attention to the corner between the first and second ramps and the heat loads on the second ramp. Information about the head loads to ramps is readily available and engineering relations exist, for example, various van Driest correlations [14–16]. Detailed investigations on the heat loads of the X-43 (Hyper-X) flight vehicle are discussed by Berry et al. [17].

Finally, CFD computations have been carried out complementary to the analysis of the measured data for a better understanding of the complex flow phenomena. The presented CFD results are 2-D and 3-D calculations performed by the numerical subproject of the research training group, including different wall temperatures [18].

II. Experimental Tools

A. Wind-Tunnel and Test Conditions

All of the experiments discussed in this paper have been performed in the hypersonic wind tunnel H2K in Cologne, Germany. The facility is a blowdown wind tunnel with test durations, depending on the flow conditions, of up to 30 s. The facility is equipped with five contoured nozzles with an exit diameter of 600 mm, that is, $M = 5.3$, 6, 7, 8.7, and 11.2. For the experiments of this study, the Mach 7 nozzle was used. To avoid condensation and to operate the wind tunnel at different stagnation temperatures, the air is heated by electrical heaters with a heating capacity of up to 5 MW. During the heating process the air is blown to the atmosphere until the desired stationary stagnation temperature is reached, subsequently a 3/2 valve is activated to let the air flow through the nozzle into the vacuum dump tank. The range of achievable Mach numbers and Reynolds numbers can be seen in Fig. 1. Reynolds numbers between 2.5×10^6 m^{-1} to 20×10^6 m^{-1} can be set by varying the stagnation pressure and stagnation temperatures.

The wind-tunnel flow conditions for the current test campaign are summarized in Table 1 and are also displayed in the performance map of the wind tunnel, Fig. 1. The dotted circles are the test conditions for the investigation of the external ramps. By far the most test runs were performed at $Re = 4 \times 10^6$ m^{-1}.

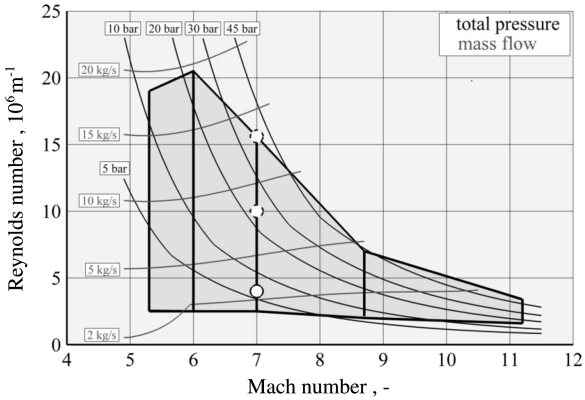

Fig. 1 Hypersonic wind-tunnel H2K, performance map.

B. Inlet Model

A newly designed model (internal name GK-01) was used in the present campaign, which has been designed based on the experience of the previously developed $M = 6$ SCR-02 model [2]. The present model has an internal contraction ratio of $I = 16\%$. This is well below the Kantrowitz and Donaldson limit [19] which is $I = 34\%$ for the corresponding lip Mach number. Thus a starting device, that is, a movable ramp or lip, is not necessary. To achieve this reduced internal compression and maintain the horizontal lip, the throat height is increased, resulting in a reduced second ramp length as seen in Fig. 2. The second ramp and the horizontal throat are connected by means of an arc. The relatively large throat height is not only a result of the desired reduced internal contraction ratio but also a result of the required combustion-chamber height.

This inlet configuration leads to a separation bubble in the throat region of the inlet based on the strong lip shock impinging on the ramp boundary layer. Concerns rose in the early phase of the project that this may lead to inlet unstart. Therefore the model was designed with an optional passive boundary layer bleed (see the dashed line in Fig. 2). The bleed gap for the discussed configuration was placed at $x = 410$ mm, with a bleed gap size of 10 mm.

The capture area A_0 of the model is 0.1×0.1 m^2 and the length to the defined interface to the combustion chamber is $L = 0.585$ m. It is equipped with a pitot rake consisting of five pitot tubes at the inlet/combustion-chamber interface, 17 static pressure ports in the upper wall of the isolator (H1–H17) and 25 pressure ports at the lower isolator wall including six pressure ports on the external ramps (R1–R25). For optical access four windows are available, which are integrated in a way that the complete internal flowpath can be observed (see Fig. 2). Compared to the previous model this model offers better measurement possibilities and more flexibility in configuration changes [2].

The inlet model itself is attached to the settling chamber of the flow meter. At the interface the transition from rectangular to round channel shape is accomplished. Depending on the optical measurement technique used the inlet is either aligned in a way that the quartz windows are visible to the shadowgraph visualization

Table 1 Wind-tunnel flow conditions

Wind-tunnel parameter	Value
Mach no. Ma_∞	**7**
Freestream pressure p_∞, Pa	**170**, 645, 890
Freestream temperature T_∞, K	**46**, 58, 55
Freestream density ρ_∞, kg · m^{-3}	**0.0123**, 0.0387, 0.0564
Total temperature T_{t0}, K	**500**, 630, 600
Total pressure p_{t0}, 10^5, Pa	**7.0**, 28.7, 40.5
Unit Reynolds no. Re_m, 10^6, m^{-1}	**4**, 10, 16

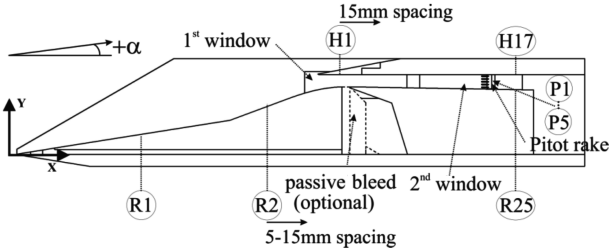

Fig. 2 Side view of the inlet model with integrated passive bleed.

setup or rotated around the x axis by 90 deg to allow optical access for the infrared system.

III. Measurement Techniques and Data Reduction

The hypersonic wind-tunnel facility uses a coincident schlieren optical setup to visualize the flow around and in the inlet model. The setup was used in shadowgraph mode for this investigation. The optical path has been modified from a prism to a beam splitter shadowgraph setup [20] based on the use of a very light sensitive charge-coupled device (CCD) camera. The static pressures as well as the pitot pressure measurements are made with the commercial Pressure Systems, Inc., 8400 system using a 64-PSI module in the present investigation.

A. Mass-Flow Meter

To measure the captured flow rate and to simulate the pressure induced by the combustion chamber, a rotational symmetric flow meter with a conical plug was used [21] and is also described in [2]. A one-dimensional flow without heat addition and sonic condition at the throat is assumed in the data reduction process.

The whole device has been calibrated in advance in accordance with DIN-1952 to achieve a relation between measured mass flow and actual mass flow as a function of throat area. In the region of interest the values of the calibration factor α vary between $0.99 < \alpha < 1.02$. The captured mass is corrected by means of this calibration function to determine the correct captured mass flow. The mass capture ratio (MCR) of the inlet is defined as

$$\mathrm{MCR} = \frac{\dot{m}_{\mathrm{mfm}}}{\dot{m}_0} = \frac{\dot{m}_{\mathrm{CC}}}{\dot{m}_0} \tag{1}$$

The calculation of the captured mass flow can be divided into three steps. First, the throat area of the flow meter is calculated based on the measured lateral position of the conical plug. Second, the Mach number M_{mfm3} ahead of the conical plug is iteratively calculated by solving the appropriate equation. Finally, the captured mass flow is calculated according to Eq. (2) using the measured static pressure p_{mfm3} in front of the conical plug, the calculated Mach number, and the known total temperature. The static pressure is measured at four locations on the circumference of the settling chamber and averaged. Based on the experience gained in the previous campaign the assumption of constant total temperature ($T_{t0} = T_{t3}$) is not valid in the H2K. Thus two thermocouples were integrated to measure the total temperature in front of the conical plug. Because the thermocouples did not reach a constant temperature until the end of a test run, the differences in total temperature at the end of all test runs were analyzed. A constant factor $F = 0.934$ could be obtained which is accurate within $\pm 1.6\%$ for all test runs of the present measurement campaign to correct the decrease in total temperature:

$$\dot{m}_{\mathrm{mfm}} = \frac{1}{F}\frac{1}{\alpha}\frac{p_{\mathrm{mfm3}}}{\sqrt{RT_{t0}}} A_{\mathrm{mfm3}} \sqrt{\kappa} M_{\mathrm{mfm3}} \sqrt{\left(1 + \frac{\kappa - 1}{2} M_{\mathrm{mfm3}}^2\right)} \tag{2}$$

The theoretically captured mass flow can be calculated by the known total wind-tunnel conditions and the capture area of the inlet. Finally, the mass capture ratio is calculated from Eq. (1).

The mass-flow meter is also used to apply different backpressures to the inlet flow. This is achieved by reducing the throat area of the flow meter. The backpressure is measured at the pitot rake position, because this is defined to be the interface location between "isolator" and "combustion chamber" and is calculated as the mean value of the upper and lower static pressure values at this location.

B. Wall Heat Flux Calculation by Means of IR Surface Temperature Measurement

For the hypersonic flight regime the knowledge of the heat loads acting on an inlet is of great importance to the overall system design, particularly for the choice of material and the cooling concept. This is especially true for the internal areas of the propulsion system because they have to be cooled, most likely regeneratively. An often used process to determine the heat flux to the wall is by measuring the surface temperature rise over time and using this data as a boundary condition for the numerical integration of the one-dimensional unsteady heat equation, normal to the surface [22]. In the present case the surface temperature distribution over time is measured with an infrared (IR) system [23] because thermocouples only measure at discrete points, and the integration into the model surface might cause problems in terms of thermal insulation as well as the heat conductivity/capacity of the thermocouple itself. Therefore a material with low heat conductivity, that is, PEEK® is inserted into the window location on one side of the inlet side walls and an IR permeable window (ZnS) on the other side wall. Because the IR camera is located inside the wind-tunnel chamber, two IR windows are placed in front of the camera, requiring a calibration of the complete optical path in front of a blackbody radiator to evaluate the right transmission coefficient and correct disturbances, that is, reflections. The data are processed and stored in a 3-D array DATA [x,y,t]. The goal of the data reduction is to know the temperature distribution perpendicular to the wall. Then the temperature gradient can be evaluated and thus the heat flux into the wall can be calculated. Here only the basic equations, Eqs. (3) and (4), are given. These equations consider the temperature-dependent material properties [22],

$$\rho(T) c_V(T) \frac{\partial T}{\partial t} = \frac{\partial}{\partial n}\left(\lambda(T)\frac{\partial T}{\partial n}\right) \tag{3}$$

$$\begin{aligned} \rho(T) c_V(T) \frac{\partial T}{\partial t} &= \frac{\partial \lambda(T)}{\partial n}\frac{\partial T}{\partial n} + \lambda(T)\frac{\partial^2 T}{\partial n^2} \\ \Rightarrow \rho(T) c_V(T) \frac{\partial T}{\partial t} &= \frac{\partial \lambda(T)}{\partial T}\left(\frac{\partial T}{\partial n}\right)^2 + \lambda(T)\frac{\partial^2 T}{\partial n^2} \end{aligned} \tag{4}$$

For external surfaces the heat radiated from the surface has to be taken into account since the convective heat from the gas to the surface is the sum of radiated and conducted heat. For internal surfaces the radiation is neglected due to the small differences in surrounding surface temperatures and the small viewing factor. Once the convective heat flux is known, the dimensionless Stanton number can be calculated.

To apply the one-dimensional approach [22] with sufficient accuracy, any heat fluxes in the plane of the investigated surface have to be minimized. This is accomplished by the use of a weak heat conducting material, that is, PEEK. This insures that the thermal gradient normal to the surface is always dominant and that the smearing of the temperature distribution can be neglected. The temperature-dependent material properties (heat conduction, heat capacity, and density) are well known, which increases the accuracy of this method. The needed material properties are available in the temperature range $300 < T < 600$ K. The accuracy of the method and the applicability for internal flowfields have been discussed in detail in the previous paper [2]. This includes the verification of the data reduction tool and the comparison of the calculated Stanton numbers by means of analytical solutions for constant Biot numbers (dimensionless heat transfer number) for a flat plate [24]. The surface

temperature development over time could be matched quite well by varying the Biot number, and the Stanton numbers calculated from this Biot number were in good agreement with the experimental results for wind-tunnel run times $t > \approx 10$ s.

Including all uncertainties into the error calculation the heat flux error itself is on the order of $\pm 5\%$ but the calculated Stanton number is in the order of $\pm 20\%$. This is mainly based on the fact that the Stanton number is very sensitive to variation in the temperature difference $(T_r - T_w)$, especially if the wall temperature approaches the recovery temperature, which is the case in the presented measurement campaign.

IV. Experimental Results of the 2-D Inlet

The main focuses of the recent experimental program are as follows:

1) to measure the effects of the integrated passive boundary layer bleed at the location of the lip shock impingement on, for example, pressure distribution, Mach number distribution, and combustion-chamber mass flow;

2) the effects of increasing the backpressure ratio on the flow structure in the isolator for the configuration without bleed;

3) the application of the infrared thermography and the calculation of the Stanton number on the external ramps and especially on the isolator side walls for different configurations and backpressures.

A. Backpressure Ratio Variation as a Function of Throttle Degree, Without and with Bleed

As mentioned previously, the mass-flow meter is also used to impose different backpressures to the internal flowfield of the scramjet compression system. The relation between the throttle degree (Δ) and the backpressure ratio can be seen in Fig. 3. Without any backpressure imposed by the mass-flow meter $\Delta < 75\%$, the static pressure ratio at the position of the pitot rake is $p/p_\infty = 30$. This value is in good agreement with the design point. The pressure ratio in general increases with increasing throttling degree. However, there is a plateau in the range of $79\% < \Delta < 83\%$, which is assumed to be due to the different shock structures in the settling chamber and the associated differences in pressure losses. A further increase in throttling degree results in an almost linear increase of the backpressure ratio. For $\Delta > 84\%$, the flow at the defined combustion-chamber interface $x = 0.585$ m is completely subsonic. At $\Delta \approx 85$–86%, which corresponds to a $p/p_\infty \approx 160$–180, there is still supersonic flow in the inlet throat and the inlet is started but all of the isolator is subsonic. The blocking limit is for approximately $\Delta > 86\%$; thereafter the backpressure ratio decreases again.

B. Experiments Without Additional Imposed Backpressure

1. Pressure and Shadowgraph Pictures

To compare the investigated inlet configurations, that is, without and with bleed, the static wall pressure distributions and shadowgraph pictures are used. The first diagram, Fig. 4a, shows the dimensionless pressure distribution for the configuration without boundary layer bleed. The theoretical value at the lip, calculated by means of simple oblique shock relations, is $c_P = 2.37$ and is plotted in the diagrams of Figs. 4a and 4b. The pressure level of the upper wall first decreases as expected; the peak in the pressure distribution (port 2, $x = 0.425$ m) indicates the shock, introduced by the separation bubble, impinging on the upper wall. Further downstream, the pressure distribution is more smooth and the typical alternating pressure peaks in the isolator are visible. These alternating peaks represent the reflected shock system propagating downstream. The separation bubble in the inlet throat has a height of about 4 mm and blocks approximately 26% of the throat height. This corresponds to an effective internal compression of $I = 37\%$ which is a bit greater than the Kantrowitz limit of $I = 34\%$. The separation bubble induced shock is clearly visible. In the vicinity of the separation bubble a very complex flowfield exists with two reflected shocks from the upper wall and one reattachment shock in the range $0.440 < x < 0.460$ m, which is reflected further downstream into the isolator. The reattachment shock leads to considerably higher pressure values compared to the situation with bleed for the three pressure ports at the lower wall near $x = 0.450$ m.

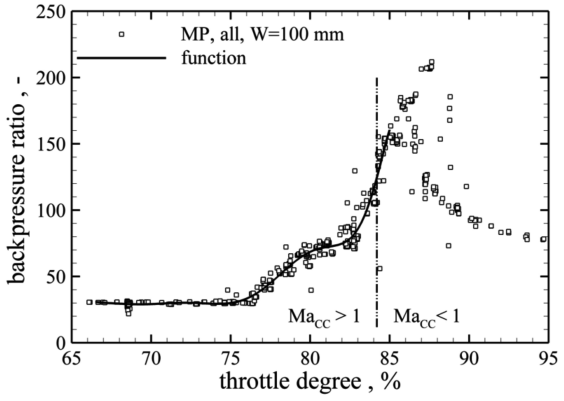

Fig. 3 Backpressure ratio as a function of throttling degree for the 2-D inlet. MP = measurement points.

In contrast to the first diagram, Fig. 4b shows the effect of introducing a passive boundary layer bleed on the viscous flow structure. Now the dimensionless pressure level of the first three pressure ports on the upper wall decrease smoothly. The distribution equals the predicted values of the method of characteristics. This implies that the shape of the lip shock is as calculated by the MOC and that no boundary layer separation on the ramp occurs. This is also obvious by looking at the shadowgraph picture. The comparison of these two diagrams shows the effectiveness of controlling the boundary layer and the shock-boundary layer interaction with the chosen design.

The change of the shock structure in the throat, that is, complex shock-boundary layer interaction with λ shock, shock–shock interaction, etc. [25], compared to a single lip shock leads to a different reflected shock structure in the isolator. This can be seen by comparing the downstream pressure ports in Figs. 4a and 4b. The strongly alternating pressure distribution in the case without bleed is not as distinct in the configuration with bleed. This is based on the fact that for the configuration without bleed the separation bubble acts as a geometrical reduced throat height. Because further downstream the isolator height is unchanged, the air is more expanded; this can be seen by comparing the solid lines (upper wall) for both configurations at $x = 0.450$ m. This leads to a greater vertical component in the velocity vector. Although the pressure variation between the upper and the lower side is greater which is based on the pressure rise at the reattachment location at the three pressure ports near $x = 0.450$ m and indicates a strong shock interaction, the reattachment shock only leads to a very small boundary layer separation, if any, on the upper wall. This may be based on the fact that the separation bubble reattachment zone gradually deflects the flow, and thus the reattachment shock is smeared and impinges weaker [25]. This is consolidated by the fact that the shock impinging angle is a bit more flat compared to the other case. Definitely the configuration without bleed results in only one main reflected shock system propagating downstream.

In contrast, the bleed introduced shock is strong enough to force the boundary layer to separate at the upper wall impinging location $x = 0.460$ m. The boundary layer is most likely turbulent although in contrast to the first case it is undisturbed up to this point. A relatively thick separation bubble emerges with limited axial dimensions. The result is a two shock system propagating downstream: the separation bubble introduced shock and the reattachment shock. This leads to a more homogeneous pressure distribution in the isolator, based on the reduced alternating y-velocity component of the main flow. Directly upstream of the pitot rake the stronger shock, originally the reattachment shock, is reflected at the upper wall leading to a clear pressure peak and the weaker shock, originally the separation induced shock, impinges on the lower wall, leading to a slightly increasing pressure distribution. Both downstream shocks are hardly visible in the shadowgraph pictures.

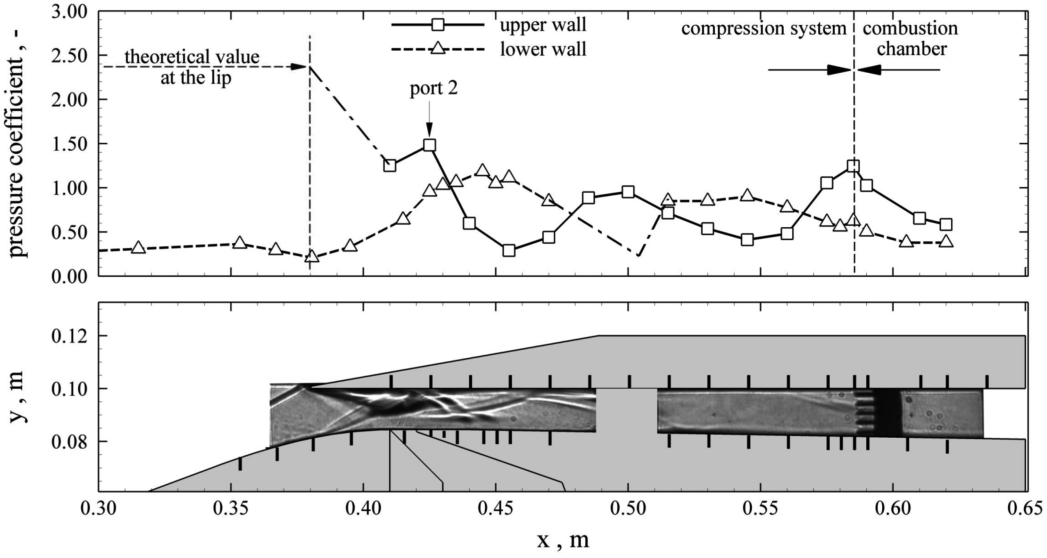

a) Static wall pressure without bleed

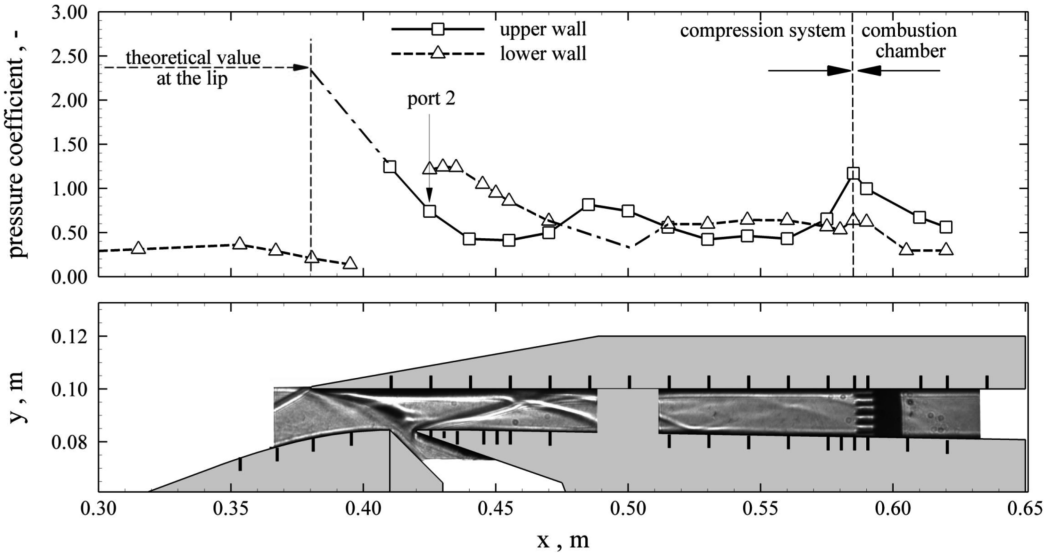

b) Static wall pressure with bleed

Fig. 4 Comparison of the static wall pressures in the isolator without and with bleed including the theoretical pressure value at the lip tip computed by oblique shock theory.

Despite the existence of the boundary layer separation in the inlet throat area, which increased the effective internal compression and caused the concern that the inlet is likely to unstart, both configurations did self start. This was discussed in detail previously and can be seen in addition by comparing the pitot pressure measurements and the calculated Mach number profiles at the isolator exit (Fig. 5), and the captured mass flows shown in Table 2. The pitot results show comparable dimensionless pitot pressure profiles. For the configuration without bleed the profile is more deformed based on the thick boundary layer on the lower wall. The profile for the configuration with bleed is a little bit more symmetric. The Mach number distributions over the height of the isolator exit at $x = 0.585$ m show comparable values and reflect the pitot pressure profiles. The Mach number is calculated using the upper wall static pressure value for the two upper pitot tubes, the lower wall static pressure value for the two lower pitot tubes and the mean value for the middle pitot tube. The error bars indicate possible variations in the static pressure value and are on the order of $\pm 5\%$. The average Mach number is on the order of $M = 2.4$ which is as desired by the combustion-chamber group within the research training group.

In Table 2, the breakdown of the different mass flows is shown. The captured mass flow for the started inlet without boundary layer bleed is $\dot{m}_{CC}/\dot{m}_0 = 0.71$ and the spill is consequently $\dot{m}_{spill}/\dot{m}_0 = 0.29$. This relatively high spill is due to the displacement effects of the thick developing boundary layers on the ramps and the side walls based on the low Reynolds number of $Re = 4 \times 10^6$ m^{-1}, the leading-edge modification with a 0.5-mm nose radius and especially due to the test Mach number of $M = 7$ that deviates from the design Mach number of $M = 7.5$. Furthermore, the lip had to be moved downstream to prevent shock impingement at different angles of attack. With the aid of computational fluid dynamics (CFD) calculations, the influence of the viscous flow on the spillage, compared to MOC design could be demonstrated. The MOC design with a sharp leading edge predicted $\dot{m}_{CC}/\dot{m}_0 = 0.82$. A 3-D Reynolds-averaged Navier–Stokes (RANS) calculation with an Speziale–Sakar–Gatski (SSG) turbulence model accomplished with the FLOWer code [18] results to a mass capture ratio of $\dot{m}_{CC}/\dot{m}_0 = 0.69$. The difference is due to the fact that the computation was fully turbulent and in the experiment the transition took place at the corner of the first and second ramps.

Because the inlet did not block for either configuration, the spill is assumed to be identical for both configurations. This leads to the result that the removed mass flow by the passive bleed is on the order of $\dot{m}_{bleed}/\dot{m}_0 = 0.02$, as shown in Table 2. The calculated mass ratios

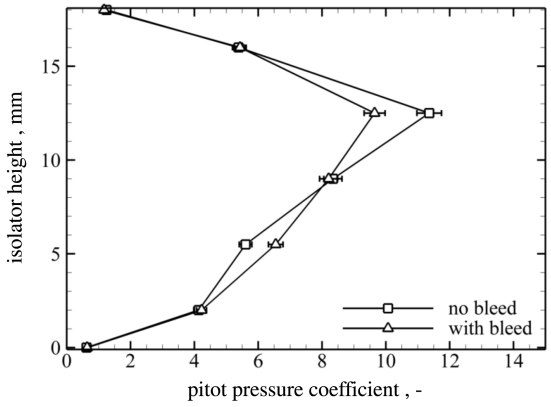

a) pitot pressure profiles

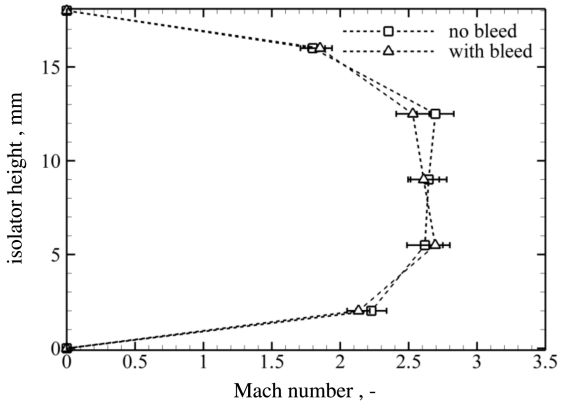

b) Mach number profiles

Fig. 5 Comparison of the pitot pressure profiles and the calculated Mach number profiles over the height of the isolator exit at $x = 0.585$ m.

for a 2-D k–ω–SST (shear stress transport) calculation accomplished with the commercial CFD tool FLUENT® for the configuration with bleed are $\dot{m}_{CC}/\dot{m}_0 = 0.77$ and $\dot{m}_{bleed}/\dot{m}_0 = 0.02$, which is in acceptable agreement with the measured values for a 2-D calculation, Table 2. But it is clear that the purely 2-D treatment of this inlet is not sufficient from a MCR point of view; the general flowfield, however, is matched quite well.

Also included in the table is the change in mass flow due to a variation in angle of attack. The angle of attack was varied in the range -3 deg $< \alpha < +3$ deg. The MCR is always calculated with the freestream mass flow through the cross-section area of the inlet (0.1×0.1 m^2) at 0-deg angle of attack. For positive angles of attack the first ramp angle is reduced which theoretically results in a decreased shock distance to the lip and thus, one could expect a higher mass capture ratio. In fact, the mass capture ratio is decreased based on the reduced freestream capture area and the movement of the lip position overcompensating the variation of the first ramp shock [26]. The definition of angle of attack is based on the orientation of the model in the wind tunnel and the fact that the propulsion unit is considered without any vehicle integration. For a possible hypersonic acceleration stage the inlet is most likely mounted on the lower side of the vehicle and is rotated 180 deg around the x axis, and thus the definition of angle of attack would be inverted.

Table 2 Breakdown of the different inlet mass flows and total pressure recovery

α, deg	Mass flow rate MCR	Bleed	Spill	π η_{KE}
0	$0.71 \pm 2.8\%$	0	0.29	0.12 0.915
+3 deg	0.56	0	0.44	——
−3 deg	0.81		0.19	
0	$0.69 \pm 2.8\%$	0.02	0.29	0.11 0.910
+3 deg	0.55	~0.02	0.44	——
−3 deg	0.80		0.19	

The total pressure recovery is difficult to measure because it is calculated from the static values at the upper and lower walls with the help of the already calculated Mach number at each pitot tube. Thereafter, the single calculated pressure recoveries are mass averaged; thus the accuracy is very limited but general conclusions can be drawn. In addition, the kinetic energy efficiency is calculated using the total pressure recovery and [10]. The pressure recovery is measured for the case with no additional imposed backpressure; thus it is representing the maximum obtainable pressure recovery of the inlet. The surprising result in the present study is that for the configuration with bleed, the pressure recovery is a little bit lower than for the case without bleed. This could be based on the above described strong bleed shock, resulting in a two shock system propagating downstream. The losses of these two shocks are apparently approximately equal to the losses generated by the separation bubble in the throat. This is in contrast to previous investigations on ramjets. The reason is probably that for ramjets the flow turns subsonic shortly after the inlet throat; thus the change in flow structure in the throat area, that is, separation bubble versus an oblique shock system, is more dominant than for scramjets where the reflected shocks in the isolator have to be considered more strongly. This effect has to be investigated in more detail, especially with the help of CFD results.

2. *Comparison Between Numerical and Experimental Results*

The following chapter shortly discusses the comparison between 2-D and 3-D numerical results obtained by university project partners and own experimental and MOC [6] results. A more detailed analysis of the numerical calculations is given in [18]. The 3-D FLOWer code solves the RANS equations and a SSG turbulent model was used. The 2-D QUADFLOW code also solves the RANS equations and a Spalart–Allmaras (SA) turbulence model was used in this case.

The agreement especially in the highly viscous dominated throat region of the inlet is very good for the 2-D and 3-D CFD calculations, Fig. 6. Especially the pressure peak at the upper wall induced by the lower wall separation shock is met very well and is an indication that the viscous effects are captured by both CFD codes in this area. The same is true for the downstream flow structure in the isolator lower wall. But for the 3-D calculations the shock impingement on the upper wall occurs further upstream than in the measured results and the 2-D CFD calculations. The reason still has to be investigated. But because this effect becomes more and more dominant downstream, the development of the 3-D corner flows and side wall boundary layer seem to be excessively considered in the 3-D CFD calculations. In addition. net refinement near the shocks has not been used yet and is a future task. The static pressure level on the upper wall at the end of the isolator is, however, better reflected in the 3-D than in the 2-D calculations.

The MOC in general represents the alternating shock structure, but the reflected lip shock impinging locations are further downstream based on the fact that by definition of the calculation method the boundary layers on the upper and lower walls and especially at the side walls are not considered in the calculation. This fact is also responsible for the discontinuous change in wall pressure at the shock impinging location. In reality, the pressure rise is smeared due to the thick boundary layer as can be seen in the measured pressure plots. The pressure rise at the upper wall in the region $0.410 < x < 0.440$ m due to the separation bubble is consequently not represented in the MOC calculations. The same is true for the pressure rise at the lower wall in the region $0.380 < x < 0.450$ m.

The pitot pressure profiles in Fig. 7a correspond quite well with each other, and because the pitot pressure is measured directly, these values are the ones to judge the numerical results. Nevertheless, the Mach number profiles are shown in Fig. 7b for comparison reasons.

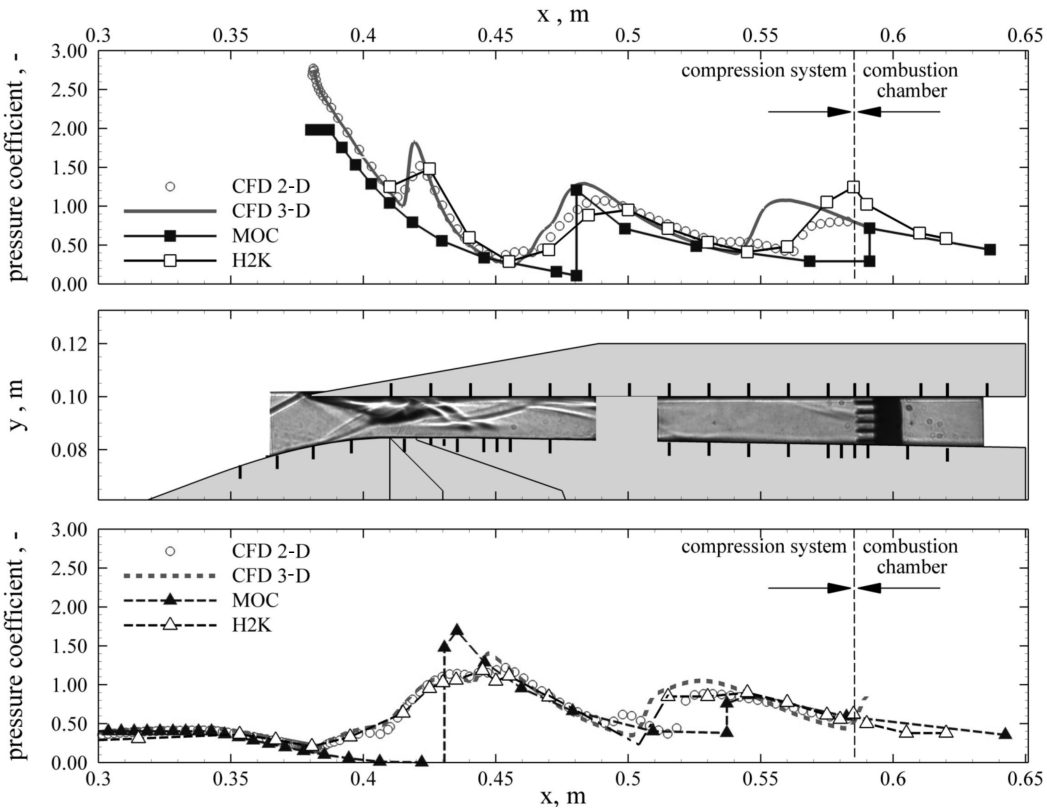

Fig. 6 Comparison of the static wall pressures in the isolator without bleed including the theoretical value computed by the MOC [6] and 2-D CFD QUADFLOW and 3-D CFD FLOWer calculations [18].

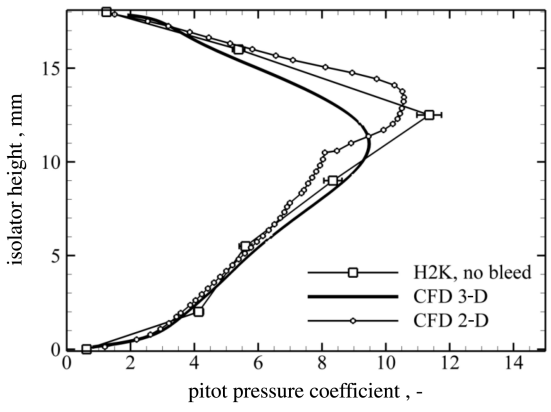

a) pitot pressure profiles

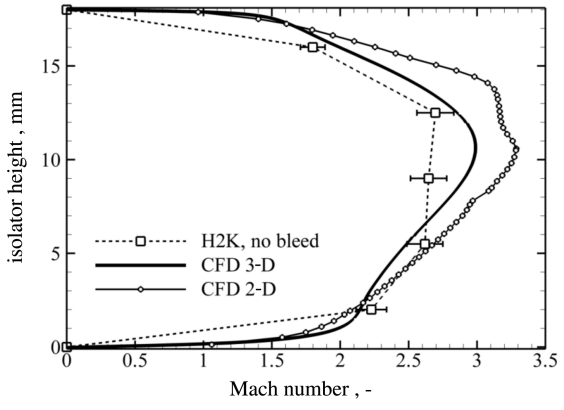

b) Mach number profiles

Fig. 7 Comparison of the pitot pressure profiles and the calculated Mach number profiles over the height of the isolator exit at $x = 0.585$ m for the measurements and for 2-D and 3-D CFD calculations [18].

The agreement is good if we consider the assumptions made for the static pressure in the data reduction of the experimental measurements. The experimentally obtained Mach numbers will be more likely closer to the higher Mach number range defined by the error bars because the pitot pressure is measured with high confidence and the made assumptions for the static pressure more likely overpredict the static pressure values. The pitot pressure peak in the upper half of the isolator is better portrayed in the 2-D calculations. On the other hand, the Mach number profile is better portrayed in the 3-D calculations. The 2-D calculation overpredicts the Mach number at the end of the isolator because the displacement effects of the corner flow and side wall boundary layer are neglected. As mentioned above a detailed discussion on the results is given in [18].

3. Infrared Measurements

After the successful application of the infrared thermography to the isolator side walls in the previous measurement campaign [2], this measurement technique has also been applied to the new model. The applicability and the feasibility of this measurement technique has been discussed previously. For the current campaign the bigger optical windows allowed the investigation of the complete internal flow structure.

The Stanton number distribution on the side wall is shown in the lower part of Fig. 8 and can be compared to the shadowgraph pictures in the upper part of Fig. 8. The varying heat transfer coefficient based on the shock structure is clearly visible. The heat loads near the lip are severe and the Stanton number reaches a value of $St = 0.022$, which is the highest value in the complete inlet for the situation without imposed backpressure. The second hot spot is the region of the reattachment shock near the lower wall at $x = 0.440$ m which corresponds very well with the shadowgraph picture shock–shock interaction and the highly measured pressure values by the ports near $x = 0.440$ m.

In the first window the shock structure is matched in the Stanton number distribution and the mean value of the Stanton number

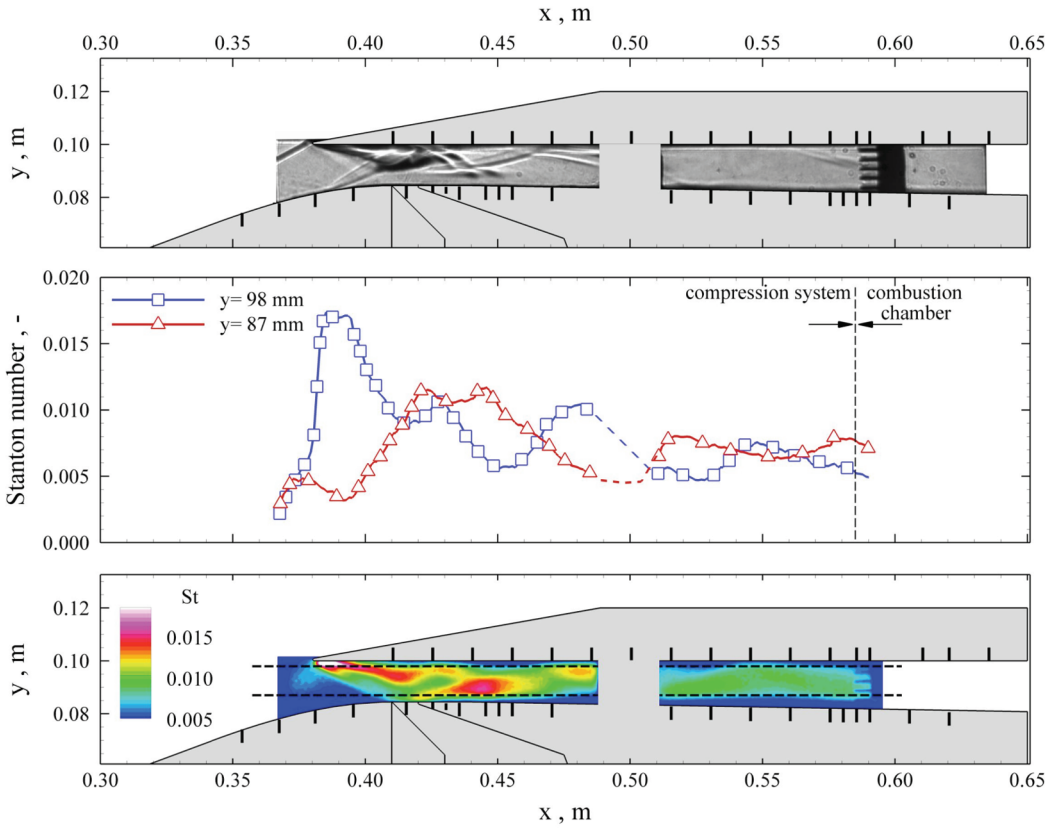

Fig. 8 Stanton number distribution on the inner side wall of the isolator; configuration without passive bleed and no imposed backpressure.

decreases further downstream. The shock structure is hard to identify based on the legend scaling. Therefore the values of the Stanton number are extracted along two lines, one close to the upper wall and one close to the lower wall. These data are also plotted in Fig. 8 and the alternating peaks, comparable to the static pressure distribution, see Fig. 4a, can be seen all the way to the end of the compression system. Compared to other heat flux measurement techniques this method has the great advantage of giving a detailed 2-D distribution of the expected heat loads and thus the cooling concept can be optimized more effectively and the evaluation of CFD codes is more meaningful.

The same diagram is shown for the configuration with bleed in Fig. 9. The change in flow structure especially in the throat location is clearly visible in the Stanton number distribution. The downstream edge of the bleed gap faces very high heat loads, comparable to the heat load at the lip. This is based on the newly developing boundary layer with very small boundary layer thickness and the high pressures present in this region (see Fig. 4b). The Stanton number inside the bleed gap is comparably low, based on the low pressure and the low mass flow in this channel. The reflection of the bleed shock at the upper wall is visible at $x = 0.470$ m, but the separation bubble and the reattachment shock cannot be resolved, at least not in the presented scaling. As mentioned previously, the pressure variations in the area of the second window are smaller and the same is also true for the Stanton number variations.

For both configurations the heat transfer coefficient decreases with increasing x coordinate. This is based on the thickening of the boundary layer which in general decreases the heat load to the wall because the temperature profile in the boundary layer and especially the temperature gradient at the wall changes. This is not true for the situation with additional imposed backpressure, as to be discussed later.

C. Experiments with Additional Imposed Backpressure

1. *Pressure and Shadowgraph Pictures*

The following section focuses on the variation of the flow structure in the rear part of the isolator. In a supersonic flow, changes in pressure cannot propagate upstream due to the parabolic character of the differential equation. However, the flow in the boundary layer eventually decelerates to subsonic velocity, thereby changing the character of the governing equations. This means that the pressure rise propagates upstream in the subsonic region of the boundary layer, resulting in a change of the complete flowfield. The positive pressure gradient forces the boundary layer to thicken and ultimately to separate. In both cases a boundary layer induced shock develops. To discuss the effects of increasing backpressure, shadowgraph pictures, Stanton number distribution, and pitot pressure profiles are shown. Because the inlet did start for the configuration without bleed, the results with different backpressures will be discussed for this configuration in the present paper.

Because of the reflected shock system in the isolator, the static pressure varies at the wall. Pressure peaks alternate between the upper and lower walls. This means that a specific pack pressure imposed to the isolator flow propagates upstream differently. At the locations where the reflected shock impinges, the backpressure is constricted from propagating further upstream based on the high pressure in this area, for example, the upper wall. By contrast, the backpressure propagates further upstream on the lower wall based on the low pressure present at the opposite side of a shock impinging location. Further increasing the backpressure leads to the situation that the backpressure overcomes the pressure at the shock impinging location and thereafter propagates far upstream, farther than on the lower wall. So the reflected lip shock system leads to a nonsymmetric shock train in the isolator (see Fig. 10). This effect reflects a real scramjet engine more realistic than ducts with a perfect parallel flow situation, as, for example, investigated by Billig [9] and Lin et al. [11] where a increase in backpressure leads to a perfect symmetric deformation of the flow, that is, the pitot pressure profile.

In Fig. 10, three different backpressure ratios are displayed. The first one is $p/p_\infty \approx 30$ ($\Delta < 74\%$) which corresponds to the cases with no additional pressure imposed to the flow and has been discussed previously (Fig. 4a). The second case represents, from a system point of view $M_{CC} > 1.8$, a possible backpressure ratio of

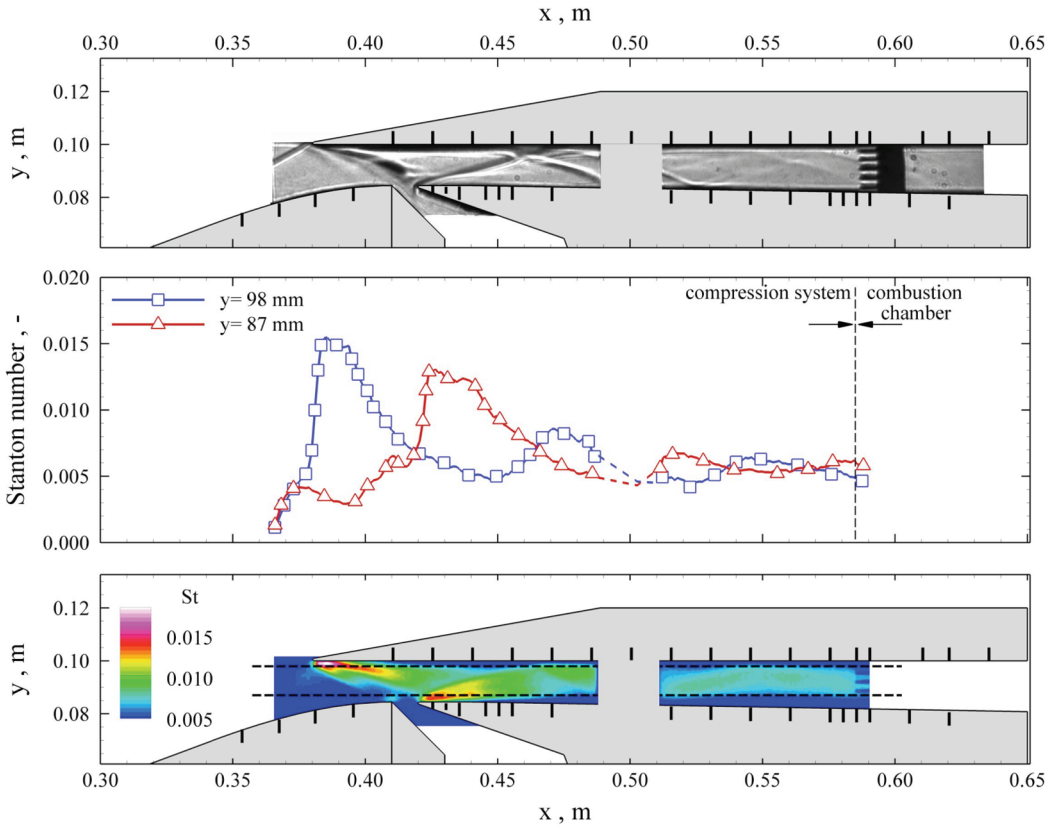

Fig. 9 Stanton number distribution on the inner side wall of the isolator; configuration with passive bleed and no imposed backpressure.

$p/p_\infty \approx 84$ ($\Delta = 83\%$). This would be the lowest allowable Mach number to enter the combustion chamber. The third case represents the transition from supersonic inflow to the combustion chamber to subsonic flow $p/p_\infty \approx 132$ ($\Delta = 84\%$).

For the $p/p_\infty \approx 84$ ($\Delta = 83\%$) case, the corresponding shadowgraph picture is displayed in the lower panel of Fig. 10. Comparing Figs. 4 and 10, the change in shock structure due to the imposed backpressure and the thickening of the boundary layer is

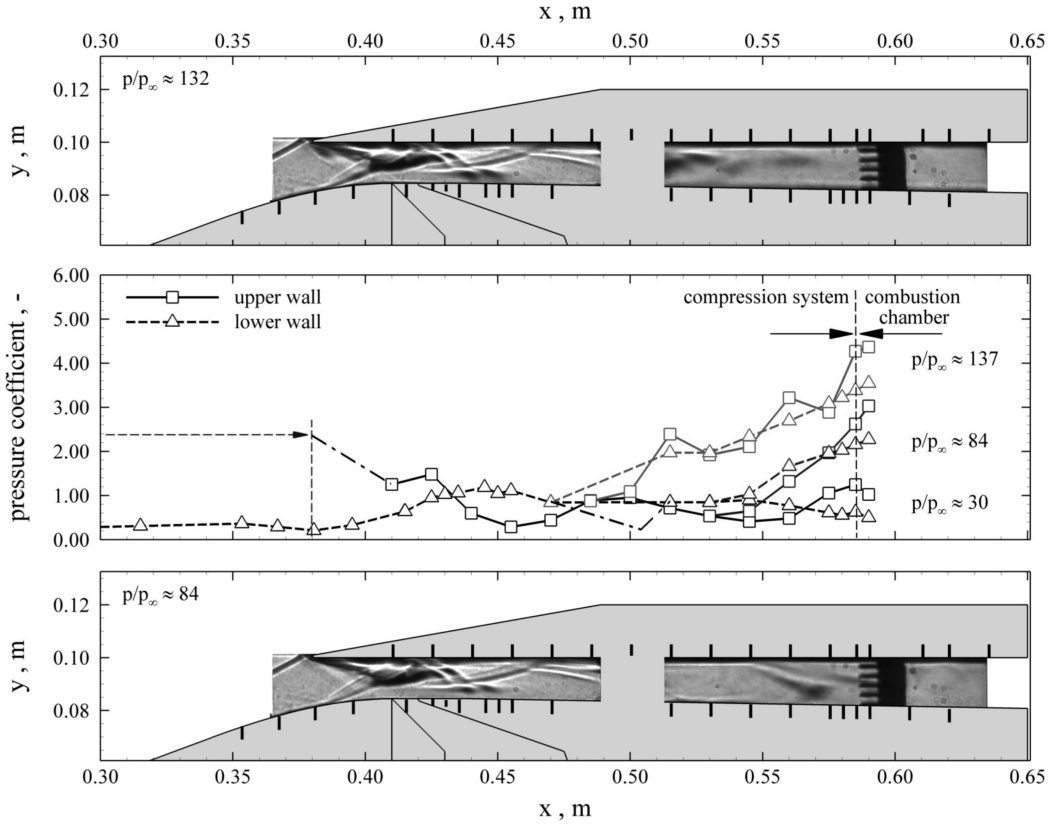

Fig. 10 Shadowgraph pictures and static wall pressure distribution for the configuration without bleed and different imposed backpressures.

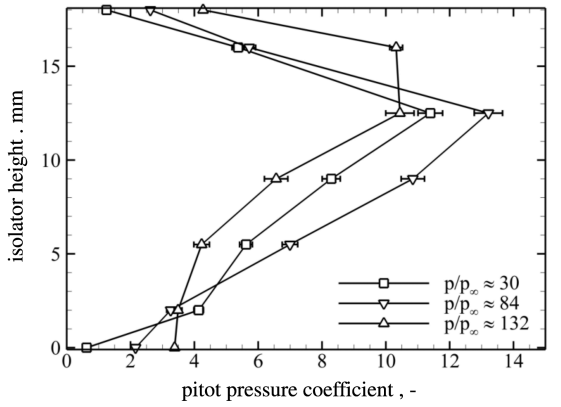

a) Pitot pressure profiles

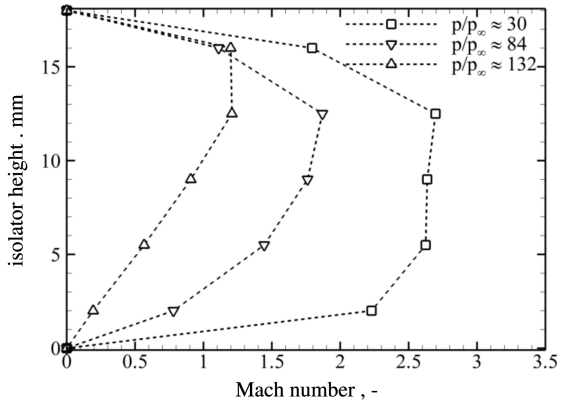

b) Mach number profiles

Fig. 11 Pitot pressure profiles and calculated Mach number profiles for the configuration without bleed and different backpressure ratios.

obvious. The pitot pressure profile, Fig. 11a, deforms mainly on the lower side of the isolator, indicating that the boundary layer thickens mainly on this side of the isolator. The maximum Mach number decreases from $M = 2.4$ to about $M = 1.8$. By comparing the pressure plots it is obvious that the shock train starts at about $x = 0.540$ m. The boundary layer induced shock on the upper side is clearly visible as well as the interaction of this shock with the boundary layer induced shock on the lower side of the isolator.

Further increasing the backpressure to $p/p_\infty \approx 132$ ($\Delta = 84\%$) pushes the shock train further upstream to about $x = 0.475$ m as can be seen in the upper shadowgraph picture and the corresponding pressure plots of Fig. 10. As in the previous case the thickening of the boundary layer occurs mainly in the lower part of the isolator as can be seen in Figs. 10 and 11. The Mach number is mainly below $M < 1$, only in the upper part of the isolator a supersonic jet is still present. The corresponding shadowgraph picture of Fig. 10 shows, in the upper half of the isolator, alternating shock structures for $0.510 < x < 0.550$ m. This shock structure is more clearly represented in the wall pressure distribution. The solid line (upper wall) has alternating pressure peaks caused by the shock train in the upper part of the isolator. In contrast, the dashed line (lower wall) rises smoothly. This, in addition to the results of the pitot rake, indicates that there is a thick boundary layer on the lower side of the isolator.

One result of this measurement campaign is the fact that the isolator length has been designed too long. The flow turns subsonic before the complete isolator contributes to the pressure rise. From a system point of view the flow should enter the combustion chamber at least with a Mach number greater than approximately $M = 1.8$. This means in the present case that only approximately 30% of the isolator is used. Thus the isolator length can be reduced by a factor of 2–3. The length based on the isolator design pressure rise of 4 is also predicted too long. Especially it seems that the calculation of the isolator exit Mach number has to be investigated in more detail. The exit Mach number has been calculated based on the impulse equation between the two sections according to [10] in the early phase of the project. The isolator exit Mach number for a pressure rise of $p_{\text{th}}/p_{\text{exit}} = 4.2$ and an assumed throat Mach number of $M_{\text{th}} = 3.46$ is $M_{\text{exit}} = 2.07$, which is too high. The isolator entrance Mach number has to be reduced to $M_{\text{th}} = 2.6$ to calculate an exit Mach number of approximately $M_{\text{exit}} = 1.3$, but then the isolator length would be $L_{\text{isolator}} = 300$ mm which would be approximately twice as much as the existing one. In contrast, using the equation proposed by Anderson [27] for one-dimensional flow with friction the Mach number at the "second" station is $M_{\text{exit}} = 1.32$ for the same pressure rise. The Mach number of $M_{\text{exit}} = 1.32$ corresponds much better to the measured values, based on the results in Fig. 11b. A pressure rise of approximately 4 corresponds to a $p/p_\infty \approx 120$, which in turn would place the Mach number profile between the two adjacent Mach number profiles in Fig. 11b, closer to the one for $p/p_\infty \approx 132$.

This means the assumptions made for the equation proposed by Billig [8] concerning the pressure rise have to be selected very carefully, especially the boundary layer assumption, isolator inflow conditions, and the adaptations from round to rectangular channel shapes [10]. The desired pressure rise could be accomplished with a shorter isolator and led to a stronger reduction in Mach number than acceptable for the combustion chamber. This is probably due to the nonuniform isolator flow as described above, the high aspect ratio of the isolator rectangle, and because of a lower throat Mach number ($M_{\text{th}} = 3.2$) than assumed at the isolator entrance. This issue has to be further investigated.

2. *Infrared Measurements*

The *infrared measurement technique* has also been used to investigate the heat loads inside the isolator at different backpressures. In Fig. 12 the Stanton number distributions are compared to the shadowgraph pictures for three different backpressure ratios. Of course, the shadowgraph measurement technique is a line of sight method and the Stanton number is evaluated by the temperature information on the side wall, but nevertheless the change in flow structure should leave one's mark at the side wall which in turn should be detectable by the infrared measurement technique.

All pictures are scaled to the same Stanton number range for comparison reasons, $0.005 < St < 0.025$. The upstream propagation of the shock train and thus the increase in heat flux to the wall is clearly visible in the Stanton number distribution. The shock structure and the Stanton number in the first window $0.370 < x < 0.490$ m do not change for these pressure ratios. In the regions affected by the backpressure rise, the Stanton number easily reaches the values at the lip. Figures 12a and 12b correspond to backpressure ratios where there is still a supersonic flow condition at the pitot rake position. In Fig. 12a the rise in Stanton number for $x > 0.540$ m matches the start of the pressure rise discussed in Fig. 10 and the change in Stanton number compared to Fig. 8 is obvious. The slightly higher values upstream are based on the reduced measurement time. The above described asymmetry in the flow structure especially for $p/p_\infty \approx 132$ ($\Delta = 84\%$) is also represented in the Stanton number distribution. The further upstream propagation of the high heat load area Fig. 12b compared to Fig. 12a corresponds also to the onset of the pressure rise in Fig. 8.

In contrast to that, the situation in Fig. 12c shows subsonic flow conditions in the rear part of the isolator for approximately $x > 0.530$ m. The Stanton numbers for $x > 0.530$ m reach very high and almost symmetrically distribute values over the complete height of the isolator on the order of $St \approx 0.026$ at the end of the isolator and are significantly higher than the values at the lip ($St \approx 0.022$). In the range of $0.450 < x < 0.530$ m the change in Stanton number and the structure due to the shock train is clearly visible. The shock train almost reaches the throat and the pressure ratio is close to the blocking limit for this inlet configuration.

As stated previously for the situation without backpressure an increase in boundary layer thickness reduces the heat load. This statement is not valid for the flow structure with imposed

backpressure. The additionally imposed backpressure indeed increases the boundary layer thickness but on the other hand the pressure is much higher and the flow is subsonic. In addition, the boundary layer is partly separated with recirculation regions for higher backpressure ratios, which is associated with very low Mach numbers (see Fig. 12b and especially Fig. 12c for the subsonic case). This means that the flow almost reaches the recovery temperature and in addition in this part of the isolator the pressure is very high, thus the heat transfer to the wall is very high. The influence of the pressure on the heat transfer is also apparent because the Stanton number in

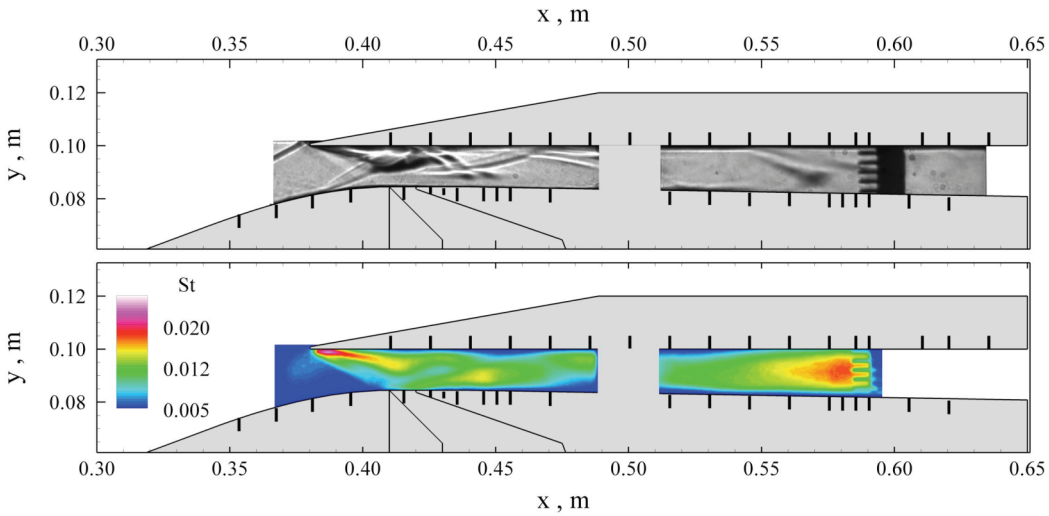

a) $p/p_\infty \approx 84$ ($\Delta = 83\%$)

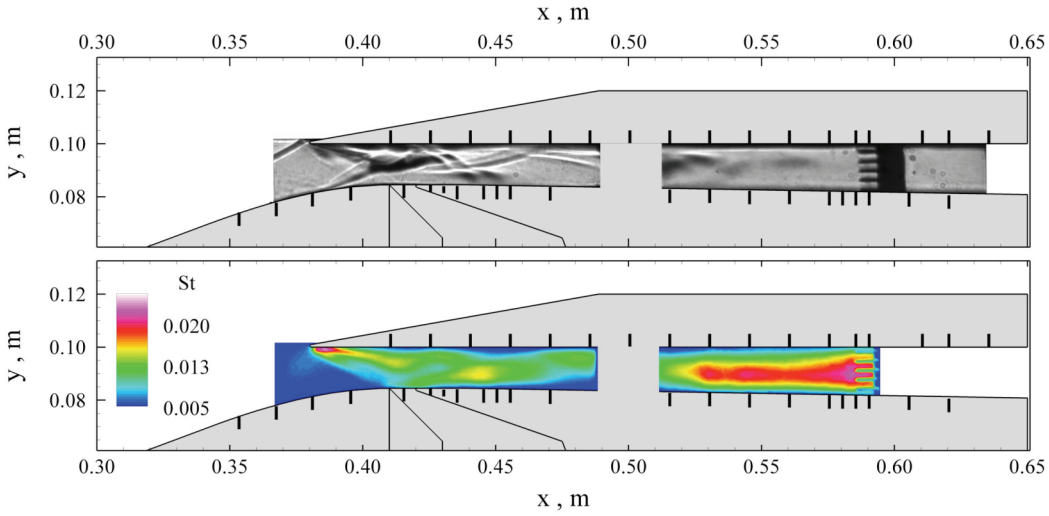

b) $p/p_\infty \approx 134$ ($\Delta = 84\%$)

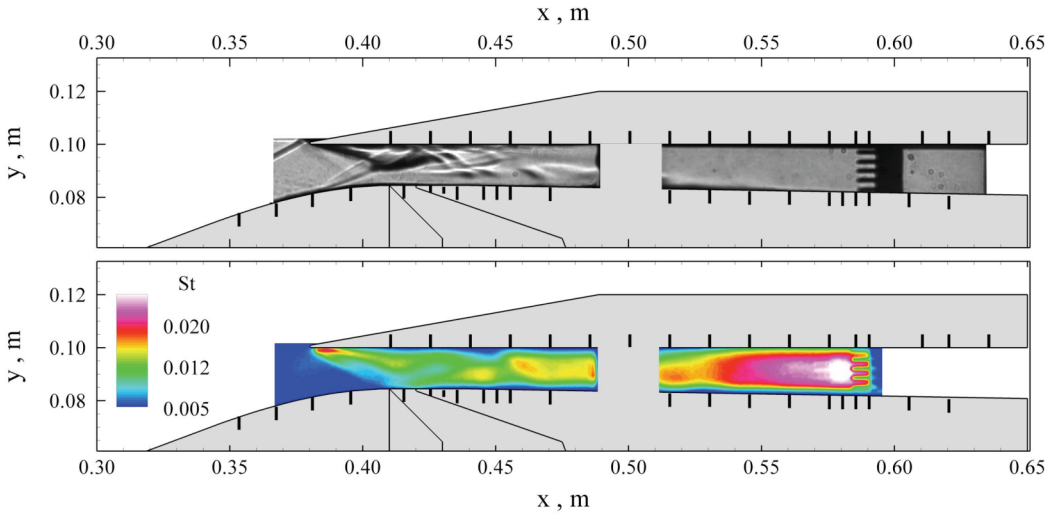

c) $p/p_\infty \approx 155$ ($\Delta = 85\%$)

Fig. 12 Shadowgraph pictures and Stanton number distribution for the configuration without bleed and different imposed backpressure.

Fig. 12c for $x > 0.540$ m rises further downstream, although the complete region is subsonic. The main parameter changing is the ongoing increase of the static pressure.

D. Flow Situation on the First and Second Ramps (Infrared Measurements)

To complete the investigation on the 2-D inlet the external ramps were investigated by means of IR thermography. The ramps were only sparsely equipped with pressure ports because the main objective was the internal flowfield of a scramjet compression system.

To check the measured IR data the Stanton number distribution along the center line is extracted and compared to the analytical solution by van Driest as reported in Korkegi [28] (see Fig. 13b for the laminar and turbulent case). For the calculation of the analytical solution the conditions behind an oblique shock were used and inserted into the according equations. Equation (5) gives the solution for the laminar case, which turned out to be the interesting one for this investigation,

$$St = \frac{0.332}{[1 + 0.032M_{\infty}^2 + 0.58(\frac{T_w}{T_{\infty}} - 1)]^{0.12} Pr^{2/3}} \frac{1}{\sqrt{Re_{\infty,x}}} \quad (5)$$

The nose radius was taken into account by virtually extending the first ramp. To do this the analytical shapes of a detached shock and an oblique shock were compared. The oblique shock was moved upstream until the detached shock far away from the round leading edge and the oblique shock coincided with each other. This extra distance was than considered in the van Driest calculation. The flow on the first ramp is clearly laminar and matches the analytical solution quite well (Fig. 13b).

Based on the low Reynolds number of only 4×10^6 m^{-1} and laminar flow on the first ramp a separation bubble exists at the interface between the first and second ramps. Obviously the ramps cannot be treated as two dimensional from this point of view and the angle between the first and second ramps of $\Delta\delta = 11.5$ deg is too large [29].

The laminar separation bubble leads to a reduced heat flux in the area of the corner. In addition, the increased heat load on the second ramp indicates a separation bubble. The heat load is higher than expected for the second ramp, based on the reattachment of the flow and introduced Görtler vortices in streamwise direction (Fig. 13a) [30,31]. The heat load decreases at the shoulder of the second ramp where the pressure decreases and the flow is accelerated and relaminarized.

Extra test runs were performed to investigate the effect of different Reynolds numbers on the separation zone and heat loads of the first and second ramps. The Reynolds number was increased to 10×10^6 m^{-1} and 16×10^6 m^{-1}. The increase by a factor of 2.5 already decreases the size on the separation bubble considerably as shown in Fig. 14a. A further increase of the Reynolds number does not result in a great change in flow topology, thus these results are not shown. The effect of variable Reynolds numbers is discussed in detail in [17] for the X-43 configuration. Because the ramp angles itself and especially

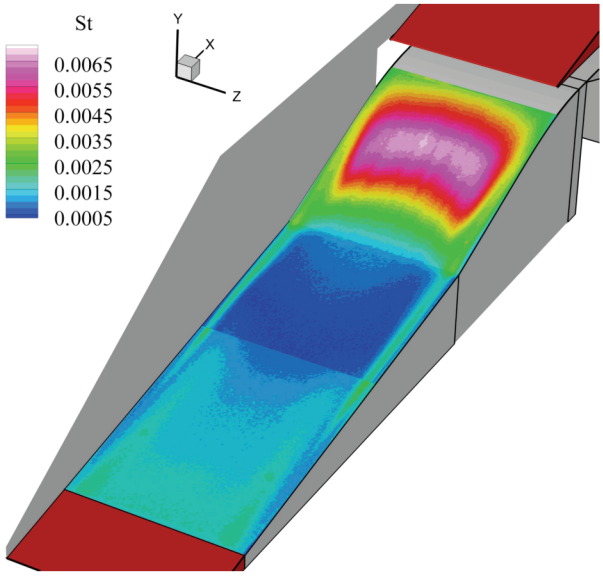

a) 3-D view of the first and second external ramps

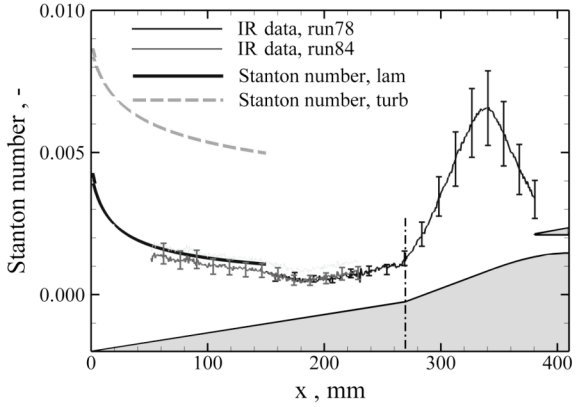

b) Stanton number along the centerline

Fig. 13 Stanton number distribution on the external ramps $Re = 4 \times 10^6$ m^{-1}, van Driest solution.

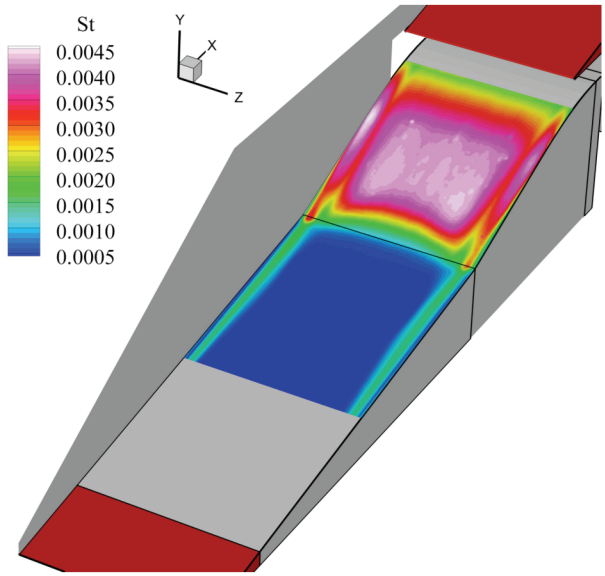

a) 3-D view of the first and second external ramps

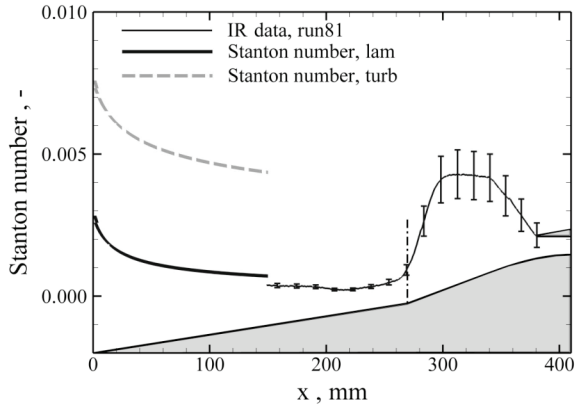

b) Stanton number along the centerline

Fig. 14 Stanton number distribution on the external ramps $Re = 10 \times 10^6$ m^{-1}, van Driest solution.

the increases from one ramp to the other are smaller, separation is limited. This is also based on the fact that the side wall starts only short in front of the lip, allowing a greater increase from one ramp angle to the other [29].

The major change in flow topology occurs between the two Reynolds numbers 4×10^6 m^{-1} and 10×10^6 m^{-1}. On the first ramp the Stanton number remains almost unchanged. In contrast to that the high Stanton number at the reattachment location on the second ramp has vanished. The Stanton number rises to a constant value considerably lower than in the previous case and decreases at the shoulder of the second ramp/throat transition. This indicates, as above, a relaminarization of the flow [30]. It seems that at a Reynolds number of 4×10^6 m^{-1}, the flow on the second ramp is transitional and becomes turbulent at higher Reynolds numbers. The moderate rise in the range of $0.270 < x < 0.290$ m is evidence to suggest that a small separation bubble is still present for the 10×10^6 m^{-1} Reynolds number case.

Because the heat loads are reduced in Fig. 14, the finer scale is more capable to resolve the corner vortices on the first ramp and especially the interaction of the corner flow with the second ramp. Here the corner vortices impinging on the second ramp result in a notable increased Stanton number in this area. In principle the same structure is present in Fig. 13 but the selected scaling is not able to resolve this. The increase in heat load in the corner region is also shown in [17,32] and is a well-known effect which has to be considered in the design. An example comparison of measured and calculated heat flux data for the ramps and corner flows of the X-43 configuration is given in Cockrell et al. [33].

V. Conclusions

The present study was motivated by the need of reliable experimental test data for the development of hypersonic scramjet propulsion units. These data do not only provide a better understanding of the viscous flow phenomena that occur in a scramjet engine; they also provide valuable data for CFD code validation. The increase in spatial resolution and the better optical access of the internal flowpath of the inlet allowed a better interpretation of the test results. The experiments successfully demonstrated that the chosen inlet design results in a starting inlet, regardless of the large separation bubble in the throat. It could be demonstrated that the size of the separation bubble can be reduced/avoided by a passive bleed with very little mass flow penalty if this should be an option from the systems point of view.

The inlet was tested at different imposed backpressures. The pressure rise without any additional imposed backpressure is $p/p_\infty \approx 30$ with a Mach number of approximately $M = 2.4$ at the isolator exit. These values correspond quite well to the expected design value. Imposing additional backpressure leads to a minimum allowable combustion-chamber entry Mach number of $M \approx 1.7$–1.8 for a pressure ratio of $p/p_\infty \approx 84$. For a pressure ratio of $p/p_\infty \approx 130$ the flow is at the transition limit from mainly super to complete subsonic flow at the combustion-chamber entrance. The inlet blocks at approximately $p/p_\infty \approx 180$. The static pressure distributions along the centerline of the upper and lower isolator walls give a detailed wall pressure plot, which could be compared with numerical calculations and are very useful for the verification of CFD codes.

For the cooling requirements of the isolator side walls and the external ramps, 2-D Stanton number distributions were obtained by infrared surface temperature measurements and a 1-D data reduction tool for the heat flux determination. These data show a detailed distribution of the Stanton number within a scramjet compression system and resolve hot spots that can help to optimize cooling concepts. In addition these data are very useful for the validation of CFD codes because the correct prediction of the wall heat flux is still challenging and depends on the selected turbulence model.

Acknowledgments

The financial support by the German National Research Council (DFG) within the research training group 1095/1 and the German Aerospace Center (DLR) Cologne is acknowledged. We would further like to thank P. Herzog and D. Lütz for their assistance during the experiments and P. Gruhn for his support during the analysis of the test results and the preparation of the paper.

References

[1] Voland, R. T., Rock, K. E., Huebner, L. D., Witte, D. W., Fischer, K. E., and McClinton, C. R., "Hyper-X Engine Design and Ground Test Program," AIAA Paper 98-1532, 1998.

[2] Häberle, J., and Gülhan, A., "Internal Flowfield Investigation of a Hypersonic Inlet at Mach 6 with Bleed," *Journal of Propulsion and Power*, Vol. 23, No. 5, 2007, pp. 1007–1017. doi:10.2514/1.29669

[3] Herrmann, C. D., and Koschel, W. W., "Experimental Investigation of the Internal Compression of a Hypersonic Intake," AIAA Paper 2002-4130, 2002.

[4] Reinartz, B. U., Herrmann, C. D., Ballmann, J., and Koschel, W. W., "Aerodynamic Performance Analysis of a Hypersonic Inlet Isolator Using Computation and Experiment," *Journal of Propulsion and Power*, Vol. 19, No. 5, 2003, pp. 868–875.

[5] Sugiyama, H., Minato, R., Minato, R., Mizobata, K., Tojo, A., and Muto, Y., "Study on Shock Wave and Turbulent Boundary Layer Interactions in a Square Duct at Mach 2 and 4," *Journal of Thermal Science*, Vol. 15, No. 1, 2006, pp. 37–42. doi:10.1007/s11630-006-0037-3

[6] Anderson, B. H., "Design of Supersonic Inlets by a Computer Program Incorporating the Method of Characteristics," NASA TN-D-4960, 1968.

[7] Van Driest, E. R., "Investigation of Laminar Boundary Layer in Compressible Fluids Using the Crocco Method," NACA TN 2597, 1952.

[8] Billig, F. S., and Kothari, A. P., "Streamline Tracing: Technique for Designing Hypersonic Vehicles," *Journal of Propulsion and Power*, Vol. 16, No. 3, 2000, pp. 465–471.

[9] Billig, F. S., "Research on Supersonic Combustion," *Journal of Propulsion and Power*, Vol. 9, No. 4, 1993, p. 499.

[10] Heiser, W. H., and Pratt, D. T., *Hypersonic Airbreathing Propulsion*, AIAA Education Series, AIAA, Washington, D.C., 1993, pp. 251–257.

[11] Lin, K. C., Tam, C. J., Jackson, K. R., Eklund, D. R., and Jackson, T. A., "Characterization of Shock Train Structures Inside Constant Area Isolators of Model Scramjet Combustors," AIAA Paper 2006-816, 2006.

[12] Kanda, T., Hiraiwa, T., Mitani, T., Tomioka, S., and Chinzei, N., "Mach 6 Testing of a Scramjet Engine Model," *Journal of Propulsion and Power*, Vol. 13, No. 4, 1997, pp. 543–551.

[13] Kouchi, T., Mitani, T., and Masuya, G., "Numerical Simulations in Scramjet Combustion with Boundary-Layer Bleeding," *Journal of Propulsion and Power*, Vol. 21, No. 4, 2005, pp. 642–649. doi:10.2514/1.7967

[14] van Driest, E. R., "The Problem of Aerothermodynamic Heating," *Aeronautical Engineering Review*, Oct. 1956, pp. 26–41.

[15] van Driest, E. R., "Turbulent Boundary Layer in Compressible Fluids," *Journal of the Aeronautical Sciences*, Vol. 18, No. 3, 1951, pp. 145–160.

[16] Tauber, M. E., "A Review of High-Speed, Convective, Heat-Transfer Computation Methods," NASA Technical Paper 2914, 1989.

[17] Berry, A. B., DiFulvio, M., and Kowalkowski, K., "Forced Boundary Layer Transition on X-43 (Hyper-X) in NASA LaRC 20-Inch Mach 6 Air Tunnel," NASA TM-2000-210316, Aug. 2000.

[18] Krause, M., and Ballmann, J., "Numerical Simulation and Design of a Scramjet Intake Using Two Different RANS Solvers," AIAA Paper 2007-5423, 2007.

[19] Kantrowitz, A., and Donaldson, C. d. P., "Preliminary Investigation of Supersonic Diffusers," NACA, ACR No. L5D20, 1945.

[20] Merzkirch, W., *Flow Visualisation*, Academic Press, New York, 1974, pp. 86–102, ISBN 0-12-491350-4.

[21] Triesch, K., "Verwendung von Kegeldüsen zur Drosselung und Durchsatzmessung bei Überschalleinläufen," German Aerospace Center (DLR), IB-39113-83-A-04, 1983.

[22] Henckels, A., and Gruhn, P., "Study on Aerothermal Effects of Viscous Shock Interaction in Hypersonic Inlets," *Proceedings of the 5th European Symposium on Aerothermodynamics for Space Vehicles*, German Aerospace Center (DLR), Cologne, Germany, 2005, pp. 553–558.

[23] FLIR Systems, ThermaCAM SC-3000. Manual, Publ. No. 557-379, June 1999.

[24] VDI-Wärmeatlas, *Berechnungsblätter für den Wärmeübergang*, 5th ed., VDI Verlag GmbH, Düsseldorf, 1988, pp. Ec1–Ec24, ISBN 3-18-400760-X.
[25] Delery, J., "Shock/Shock and Shock-Wave/Boundary-Layer Interactions in Hypersonic Flows," AGARD FDP-VKI, 30 May–3 June 1988.
[26] Hermann, D., Triesch, K., and Gülhan, A., "An Experimental Study of Chin-Intakes for Airbreathing Missiles with High Agility," *Journal of Propulsion and Power* (to be published).
[27] Anderson, J. D., Jr., *Modern Compressible Flow*, 2nd ed., McGraw–Hill, New York, 1982, pp. 85–91, ISBN 0-07-001673-9.
[28] Korkegi, R. H., "Training Center for Experimental Aerodynamics," Course Note 9, *Hypersonic Aerodynamics*, Rhode-Saint-Genes, Belgium, 1962, pp. 120–128.
[29] Korkegi, R. H., "Comparison of Shock-Induced Two- and Three-Dimensional Incipient Turbulent Separation," *AIAA Journal*, Vol. 13, No. 04, 1975, pp. 534–535.
[30] Hirschel, E. H., *Basics of Aerothermodynamics*, jointly published with the AIAA, Springer–Verlag, Berlin Heidelberg, 2005, pp. 199–310, ISBN 3-540-22132-8.
[31] Henckels, A., and Gruhn, P., "Basic Research and Technologies for Two-Stage-to-Orbit Vehicles," Wiley-VCH Verlag GmbH & Co., Weinheim, Germany, 2005, Chap. 5, pp. 383–403, ISBN 13: 978-3-527-27735-3.
[32] Steinback, P. C., and Weinstein, L. M., "Aerodynamic Heating in the Vicinity of Corners at Hypersonic Speeds," NASA TN-D-4130, 1967.
[33] Cockrell, C. E., Auslender, A. H., White, J. A., and Dilley, A. D., "Aeroheating Predictions for the X-43 Cowl-Closed Configuration at Mach 7 and 10," NASA Langley Research Center, Hampton, VA, AIAA Paper 2002-0218, 2002.

R. Bowersox
Associate Editor